

EXTRACTION OF BLOOD DROPLET FLIGHT TRAJECTORIES FROM VIDEOS FOR FORENSIC ANALYSIS

L. A. Zarrabeitia, D. A. Aruliah and F. Z. Qureshi

Faculty of Science, University of Ontario Institute of Technology, Oshawa, ON, Canada

Keywords: Stereo reconstruction, Tracking, Droplets, Blood flight, Multi-target tracking.

Abstract: We present a method for extracting three-dimensional flight trajectories of liquid droplets from video data. A high-speed stereo camera pair records videos of experimental reconstructions of projectile impacts and ensuing droplet scattering. After background removal and segmentation of individual droplets in each video frame, we introduce a model-based matching technique to accumulate image paths for individual droplets. Our motion detection algorithm is designed to deal gracefully with the lack of feature points, with the similarity of droplets in shape, size, and color, and with incomplete droplet paths due to noise, occlusions, etc. The final reconstruction algorithm pairs two-dimensional paths accumulated from each of the two cameras' videos to reconstruct trajectories in three dimensions. The reconstructed droplet trajectories constitute a starting point for a physically accurate model of blood droplet flight for forensic bloodstain pattern analysis.

1 INTRODUCTION

Bloodstain pattern analysis (BPA) comprises techniques for inferring spatial locations of bloodletting events from bloodstains found at crime scenes (Bevel and Gardner, 2008; Buck et al., 2011). At present, BPA, to a large extent, is a qualitative sub-discipline of forensic science. Our present goal is to improve computational models for bloodletting events and bloodstain pattern formation. These models, we believe, will be of immense value to forensic investigators and BPA specialists for reasoning accurately from images of bloodstain patterns at crime scenes. Furthermore, such models are required to develop the next generation of BPA software for inference and assessing uncertainties in BPA.

Stringing (Buck et al., 2011) is a common method for locating the bloodletting event responsible for a particular bloodstain pattern. This method relies on the assumption that blood droplets move in straight lines, ignoring the effects of gravity and aerodynamic drag. Stringing can provide reasonable approximate locations projected onto a horizontal plane. At short distances, stringing may also provide estimates for the height of the bloodletting event. More accurate ballistic models that incorporate viscous drag forces and gravity, are only used when the stringing method produces unreasonable locations or speeds (Buck et al., 2011). Our results suggest that the effects of gravity and drag are noticeable, even over the short distances

and time scales recorded in our experiments.

The present work is concerned with reconstructing 3D trajectories of blood droplets from high-speed video data. We have developed a stereo vision system capable of tracking individual blood droplets in high-speed videos (1300 frames per second) and automatically reconstructing their three-dimensional (3D) flight trajectories. In each experiment, the stereo camera pair captures a high-speed video of the impact of a BB pellet with a ballistic gel encasing transfer blood (i.e., approximating human flesh); this scenario is intended to simulate a penetrating trauma (e.g., a gunshot wound). Upon impact, the ballistic gel is punctured and expels its contents at high speeds. Blood droplets then fly through the air hitting nearby surfaces to create bloodstain patterns. Our video recordings of these simulated bloodletting events allow us to study the effects of gravity and aerodynamic drag on blood droplet trajectories (see Figure 1). We also photograph the resulting bloodstain patterns.

Estimation of individual blood droplet trajectories from recorded videos comprises three stages:

1. subtracting the background and connected-component analysis to identify images of individual blood droplets in each video frame;
2. tracking of individual blood droplets between video frames to generate 2D droplet in each camera's view; and
3. estimating three-dimensional trajectories by link-

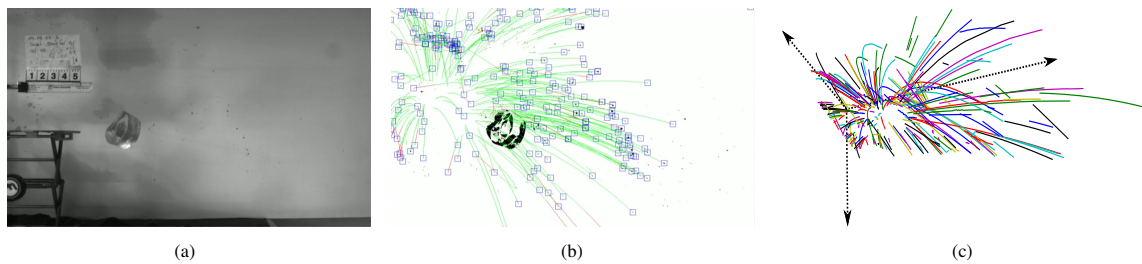


Figure 1: (a) BB pellet impacting ballistic gel containing transfer blood. (b) Tracking individual blood droplets in high-speed video (1300 frames per second). (c) Reconstructed blood droplet trajectories. Notice the effects of gravity and viscous drag forces even for short trajectories.

ing image paths from each camera’s view.

We present a model-based approach to tackle this challenging problem.

The long-term goal that motivates the present study is to develop accurate physics-based models of blood flight to reconstruct impact conditions in blood-stain pattern analysis. As a first step, then, we record and compare flight patterns with models traditionally used in this field. Thus, we automate the extraction and synthesis of 3D trajectories of individual droplets from video recordings.

1.1 Related Work

While object-tracking has been studied extensively within the computer vision community (see, e.g., (Yilmaz et al., 2006)), tracking flight paths of liquid droplets across a large number of frames of video presents considerable challenges. In particular, tracking individual blood droplets involves identifying hundreds of semi-transparent, quasi-deformable objects of very similar sizes and appearances. Tracking can be formulated by establishing correspondences between detected objects represented by points (or targets) across frames. Point correspondence is a complicated problem, especially in the presence of occlusions, misdetections, and objects entering or leaving the field of view. The most obvious difficulty in our problem arises from the similarity between blood droplets; tracking techniques based on detection of feature points (such as in (Yilmaz et al., 2006)) are not effective in this context. We apply an approach similar to that followed in (Balch et al., 2001) to detect individual blood droplets in each of the video frames captured by each camera. The problem in this earlier work is similar to ours, albeit with fewer targets and greater information in each frame.

A core requirement of tracking algorithms is solving assignment problems to match objects between successive video frames. The Kuhn-Munkres Algorithm (also known as the Hungarian algorithm (Kuhn, 1955; Munkres, 1957)) was proposed in the

mid-1950s to solve linear assignment problems in polynomial time. Bourgeois and Lassalle extended the Kuhn-Munkres algorithm to handle rectangular problems in 1971 (Bourgeois and Lassalle, 1971). A more recent effort, in addressing the sailor assignment problem, produced a variant of the rectangular method for sparse graphs and multiobjective problems (Dasgupta et al., 2008). For more recent surveys of rectangular assignment problems in the context of multiple target tracking and in general, see (Poore and Gadaleta, 2006) and (Bijsterbosch and Volgenant, 2010).

Among algorithms proposed to solve the problem of multi-target tracking are MHT (Reid, 1979) and Greedy Optimal Assignment (Veenman et al., 2001). The latter is used in (Betke et al., 2007) to track a large number of bats. A similar strategy is used in (Balch et al., 2001) for tracking the behaviour of live insects. In (Khan et al., 2003) and (Khan et al., 2005a), the authors propose a particle filter for tracking the motion of insects. Both of these studies involve applying a Markov field to model insect interactions and assuming that the targets actively avoid collisions. (Khan et al., 2005b) extends these works to deal with split and merged measurements. A problem similar to ours is studied in (Grover et al., 2008) and (Straw et al., 2011). They succeed in reconstructing the 3D trajectories of multiple targets — in these instances, flies — from a multi-camera setup. The movements of insects are arguably harder to predict than the ballistic trajectory of blood droplets. On the other hand, the insect-tracking problem is less sensitive to errors in prediction as there are fewer targets moving at lower speeds and the number of targets does not change (as compared to flying droplets that can split and merge).

2 BACKGROUND REMOVAL AND SEGMENTATION

The cameras detect minute lighting fluctuations be-

tween frames due to the high frame-rate even under carefully controlled conditions. As such, we employ a dynamic background model (Balch et al., 2001) to identify pixels corresponding to blood droplets. Once the background is subtracted, a binary mask is superimposed to identify target clusters of pixels that ostensibly correspond to fluid droplets.

2.1 Identifying the Background

Our proposed dynamic background model successfully compensates for noticeable fluctuations in overall image intensity between successive frames. Let $I^{(k)}$ denote the image intensity in the k^{th} video frame and let $B^{(k)}$ denote the corresponding background model. Both $I^{(k)}$ and $B^{(k)}$ are matrices with real-valued entries between 0.0 and 1.0. We also construct the corresponding binary mask $F^{(k)}$ (i.e., a matrix with 0-or-1 entries) to indicate pixels in frame k associated with blood droplets (see Figure 2).

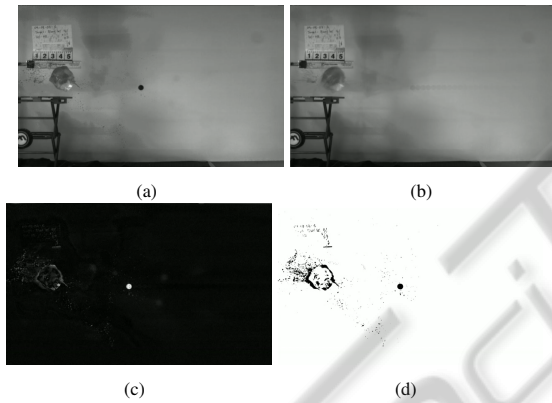


Figure 2: Blood droplet segmentation: (a) Original image intensity $I^{(k)}$. (b) Background model $B^{(k)}$. (c) Deviation from the background model $|I^{(k)} - B^{(k)}|$. (d) Foreground mask $F^{(k)}$.

The aforementioned lighting fluctuations preclude using a constant background model $B^{(k)} = B^{(0)} = I^{(0)}$ in all frames. Instead, we apply the dynamic linear model

$$B^{(0)} = I^{(0)}, \quad (1a)$$

$$B^{(k+1)} = (1 - \alpha)B^{(k)} + \alpha I^{(k)}, \quad \alpha \in [0, 1]. \quad (1b)$$

The coefficient α in (1b) controls how quickly the background model adapts to the changes in the background (e.g., newly formed bloodstains on the back wall). Small values of α imply a slow learning speed. For example, when $\alpha = 0$, the result is a constant background model; such a model is incapable of dealing with changes in illumination or in the background. Conversely, large values of α may cause the moving

droplets to be considered part of the background; this leads to a ghosting effect where droplets are detected twice in each frame. More sophisticated techniques (e.g., random Markov fields) could alternatively be used for background subtraction; however, in this application context, such models unnecessarily introduce additional complexity without significant gain.

Having determined the background model $B^{(k)}$ in the k^{th} frame, the binary mask $F^{(k)}$ is computed pixel-wise by the rule

$$F^{(k)}(u, v) = \begin{cases} 1 & \text{if } |I^{(k)}(u, v) - B^{(k)}(u, v)| > \epsilon_{\text{bg}}, \\ 0 & \text{otherwise.} \end{cases} \quad (2)$$

The preselected threshold value $\epsilon_{\text{bg}} \in [0, 1]$ in (2) has to be chosen carefully. The challenge is to ensure capturing droplets flying over darker regions of the background, while ignoring intensity fluctuations between frames.

Suitable values of α and ϵ_{bg} cannot generally be determined *a priori*; they depend on ambient experimental conditions indiscernible by the naked eye. This problem can be alleviated, but not completely solved, by previewing a few frames taken at high speed prior to the experiment. Previewing a few frames allows us to relocate the lights to maximize contrast and reduce shadows.

2.2 Segmentation of Individual Droplets

The process of background removal yields a sequence of binary masks $\{F^{(k)}\}_{k=0}^{N_{\text{frames}}}$. From the binary mask $F^{(k)}$ of the k^{th} video frame, the clusters of pixels in the connected components of $F^{(k)}$ correspond to individual foreground objects. Some of these clusters correspond to genuine blood droplets, but some others are false positives (e.g., the projectile, falling gelatin, and noise or illumination artifacts). False positives are filtered out by discarding clusters that are either too big or too small. We refer to the pixel clusters associated with blood droplets as *targets* and we denote the set of all targets accepted in frame k by $T^{(k)}$.

Each target $\mathbf{t} \in T^{(k)}$ has a number of properties that are recorded. For instance, the target \mathbf{t} has an area a (in pixels) and associated raw moments M_{00} , M_{01} , and M_{10} (see, e.g., the documentation of OPENCV (Bradski, 2000) for appropriate definitions). The moments of \mathbf{t} are required to compute the image coordinates of the target's centroid (\bar{u}, \bar{v}) which is considered the location of the blood droplet associated with the target. These properties are recorded for each target in each frame and are used to match targets in successive frames for motion tracking.

3 TRACKING TARGET PATHS IN IMAGES

Tracking the motion of an object using video data entails identifying images of the same points (targets) in a sequence of successive frames. When dealing with small numbers of easily distinguishable rigid objects (e.g., when colour and shape are clearly distinct or when obvious feature points are available), associating targets from frame to frame is straightforward. However, when trying to track large collections of very similar objects, more sophisticated measures are needed to assess the credibility of the reconstructed motion of individual targets.

3.1 Limitations of Tracking Targets Strictly Frame-by-frame

To state the tracking problem in concrete terms, recall that $T^{(k)}$ denotes the set of all targets (images of droplets) detected in frame k . Each target in $\mathbf{t}^{(k)} \in T^{(k)}$ can be thought of as a pair $\mathbf{t}^{(k)} = (\bar{u}^{(k)}, \bar{v}^{(k)})$ of pixel coordinates (given by the target's centre of mass). Targets have additional properties other than their centroids (e.g., areas, moments, etc.) that can be used in tracking. Many tracking algorithms (e.g., in (Balch et al., 2001)) are based on linking targets in $T^{(k)}$ (i.e., from frame k) directly to targets in $T^{(k+1)}$ (i.e., from frame $k+1$).

Such approaches work well when the cardinality of the target sets does not vary significantly between frames. For the droplet tracking problem, this assumption breaks down in a number of ways:

1. a false target $\mathbf{t}^{(k)}$ is spuriously detected in frame k , i.e., pixels contaminated by noise are mistaken for a legitimate physical object in the scene;
2. a true target $\mathbf{t}^{(k)}$ is not detected by the camera in frame $k+1$;
3. a true target $\mathbf{t}^{(k)}$ is temporarily occluded by another object in frame $k+1$;
4. a target $\mathbf{t}^{(k)}$ temporarily leaves the field of view between frames k and $k+1$;
5. a target $\mathbf{t}^{(k+1)}$ returns to the field of view between frames k and $k+1$;
6. a target $\mathbf{t}^{(k)}$ permanently leaves the field of view between frames k and $k+1$; and
7. a target $\mathbf{t}^{(k+1)}$ initially enters the field of view between frames k and $k+1$.

These modes of failure are the norm rather than exceptions. In case (1), it is necessary to handle spurious detections gracefully. The cases (2), (3), and (4)

are temporary failures; it is best not to match the target $\mathbf{t}^{(k)} \in T^{(k)}$ with any target in $T^{(k+1)}$. Similarly, in case (5) when the target $\mathbf{t}^{(k+1)}$ is detected again in frame $k+1$, it should be paired with a candidate from a frame prior to frame k (i.e., the most recent frame in which the corresponding droplet was detected). Finally, the situations (6) and (7) should be considered only when there is no suitable candidate target in any later or earlier frames respectively.

3.2 Assignment Problems for Tracking

We modify the formulation of the tracking problem to allow for the difficulties outlined in Section 3.1. The key problem that needs to be solved at each stage is an *assignment problem*. Assignment or matching problems constitute a fundamental class of problems in combinatorial optimization. In specific language, let A and B be finite sets (i.e., vertices of a bipartite graph), let $\text{cost} : A \times B \rightarrow \mathbb{R}$ be a cost function associated edges between A and B , and let $\mathcal{M} \subset \mathcal{P}(A \times B)$ be a proper subset of the power set $\mathcal{P}(A \times B)$. The *Assignment Problem (AP)* is to construct a matching $M \subset A \times B$ such that the total cost summed over all edges in M is minimized, i.e.,

$$\min_{M \in \mathcal{M}} \sum_{(a,b) \in M} \text{cost}(a,b). \quad (3)$$

If $|A| = |B|$ are equal and \mathcal{M} consists of all possible matchings that cover both A and B , the problem (AP) is called a Linear Assignment Problem (LAP). If $|A| \neq |B|$, and \mathcal{M} consists of all matchings that cover the smaller set, the problem (AP) is called a Rectangular Linear Assignment Problem (RLAP). Observe that the constraint \mathcal{M} on the set of possible matchings is necessary; otherwise, for many cases, the minimizer would simply be the empty matching $M = \emptyset$.

Assuming for the moment that the constraint $\mathcal{M} \subset \mathcal{P}(A \times B)$ is known, we shall assume henceforth that

$$"M = \text{SolveAP}(A, B, \text{cost}, \mathcal{M})" \quad (4)$$

means "Solve (AP) by computing the matching $M \in \mathcal{M}$ that minimizes the sum in (3)." We implicitly assume that a solution of (AP) exists as does a reasonable algorithm for computing it. For all practical purposes, we use the techniques in (Dasgupta et al., 2008) to compute M in (4).

In some cases of (AP), not all edges are present in the bipartite graph, i.e., some of the elements of A are not connected to elements of B . This assignment problem can still be solved using a variant of the Kuhn-Munkres algorithm that assigns (practically) infinite cost to absent edges (see (Dasgupta et al., 2008)). The missing edges also introduce the constraint $\mathcal{M} \subset \mathcal{P}(A \times B)$.

As an example of an assignment problem in tracking, the approach followed by (Balch et al., 2001) is to find, at step k , a matching

$$M^{(k)} = \text{SolveAP}(T^{(k)}, T^{(k+1)}, \text{dist}, \mathcal{M}), \quad (5)$$

where \mathcal{M} consists of all matchings that cover either $T^{(k)}$ or $T^{(k+1)}$ and

$$\text{dist}(\mathbf{t}^{(k)}, \mathbf{t}^{(k+1)}) = \|\mathbf{t}^{(k)} - \mathbf{t}^{(k+1)}\|_2^2. \quad (6)$$

There is no problem computing the cost for any edge since it is merely the Euclidean distance.

In our formulation, we solve an assignment problem (3) where “A” is a set of *paths* and “B” are *targets* (rather than targets and targets as in (Balch et al., 2001)). To the best of our knowledge, this formulation differs from previous tracking work that matches targets strictly between subsequent frames. Specifically, a *path* is an ordered list of one or more targets $[\mathbf{t}^{(k_1)}, \mathbf{t}^{(k_2)}, \dots, \mathbf{t}^{(k_s)}]$ occurring in a strictly increasing sequence of frames (i.e., so that $k_1 < k_2 < \dots < k_s$). Notice that we do not require that successive targets in a given path occur in successive video frames (i.e., that $\mathbf{t}^{(k)} \in T^{(k)}$ absolutely must be followed by some $\mathbf{t}^{(k+1)} \in T^{(k+1)}$) as we wish to deal with situations enumerated in Section 3.1 gracefully. With this terminology, we consider a set $P^{(k)}$ of paths linking targets in a strictly increasing subsequence drawn from the 0th frame up to and including the k^{th} frame.

Our multi-target tracking problem can then be expressed recursively using the solution of an assignment problem at each step. In particular, the desired matching is

$$M^{(k)} = \text{SolveAP}(P^{(k)}, T^{(k+1)}, \widehat{\text{dist}}, \widehat{\mathcal{M}}), \quad (7)$$

where $\widehat{\text{dist}}$ is defined using a path-based predictive model described in Section 3.3. The set $\widehat{\mathcal{M}}$ is a little harder to describe; it consists of matchings M with the property that, if $\widehat{\text{dist}}(p, t) < \infty$, then M covers at least one of p or t (but not necessarily both).

3.3 A Model-based Distance Metric

We do not solve the assignment problem by minimizing a sum of Euclidean distances between targets in successive frames as in (6). Instead, we track target motion by minimizing the distances between targets in the next frame and targets *predicted using the paths*. Predictive algorithms usually include a step in which a model for each target’s motion is learned (e.g., by a Bayesian network (Nillius et al., 2006) or a Kalman Filter (Iwase and Saito, 2004)). In the present context, we exploit basic models of droplet motion.

Projectiles follow simple parabolic trajectories (with constant horizontal speeds and constant vertical acceleration $g \simeq 9.81 \text{ms}^{-2}$) in the absence of aerodynamic drag forces. The projection of such ballistic trajectories in the image plane are similarly quadratic curves. Even accounting for viscous drag effects, over sufficiently short time intervals (as is the case for high-speed video), quadratic polynomials provide robust approximations.

Thus, given a path $p \in P^{(k)}$ corresponding to some droplet’s partial motion up to and including frame k , the estimated image coordinates of the target in frame $k+1$ are given by

$$\hat{\mathbf{t}}_p^{(k+1)} = \begin{pmatrix} \hat{u}_p^{(k+1)} \\ \hat{v}_p^{(k+1)} \end{pmatrix} = \begin{pmatrix} a_u \tau_{k+1}^2 + b_u \tau_{k+1} + c_u \\ a_v \tau_{k+1}^2 + b_v \tau_{k+1} + c_v \end{pmatrix}, \quad (8)$$

where τ_{k+1} is the time corresponding to frame $k+1$. The coefficients a_u , a_v , b_u , b_v , c_u , and c_v are determined using standard polynomial least-squares fitting based on the targets in the path p . In the first few frames, if a least-squares quadratic cannot be used to fit targets in path p , polynomials of degree 0 or 1 are generated to predict $\hat{\mathbf{t}}_p^{(k+1)}$ instead.

Given a path $p \in P^{(k)}$, the predicted target $\hat{\mathbf{t}}_p^{(k+1)}$ from (8) is used to define the modified cost function $\widehat{\text{dist}}$ in (7) for match p to targets in $T^{(k+1)}$. To evaluate a proposed matching $M^{(k)} \subseteq P^{(k)} \times T^{(k+1)}$, the cost function is given by

$$\widehat{\text{dist}}(p, \mathbf{t}^{(k+1)}) = \|\mathbf{t}^{(k+1)} - \hat{\mathbf{t}}_p^{(k+1)}\|_2^2. \quad (9)$$

That is, when comparing different assignments of paths $p \in P^{(k)}$ to candidate targets $\mathbf{t}^{(k+1)} \in T^{(k+1)}$, this cost function penalizes targets that deviate too much (in Euclidean distance) from the prediction $\hat{\mathbf{t}}_p^{(k+1)}$.

3.4 A Predictive Tracking Algorithm

With an explicit specification of the prediction strategy (8) and the cost function (9), we can now provide a high-level description of our approach to tracking targets through the video data in Algorithm 1.

Observe that, rather than keeping track of individual collections of paths $P^{(k)}$, all the paths are simply accumulated into a single set. The loop at line 4 accumulates a set of candidate matches for p in S ; corresponding edges are added to $E^{(k)}$ in line 7. The purpose of accumulating $E^{(k)}$ is for various performance enhancements exploiting sparsity for solving (7) for the matching $M^{(k)}$ at line 8 (as in (Dasgupta et al., 2008)). The final loop at line 9 extends the paths p covered by $M^{(k)}$ once the matched targets $\mathbf{t}^{(k+1)} \in T^{(k+1)}$ have been determined. Finally,

Algorithm 1: Tracking and assembling image paths.

Input: Set of targets in each frame $\{T^{(k)}\}_{k=0}^{N_{\text{frames}}}$
Output: Set P of (possibly incomplete) paths

- 1: $P \leftarrow \{[\mathbf{t}^{(0)}] \mid \mathbf{t}^{(0)} \in T^{(0)}\}$ {singleton lists}
- 2: **for** $k = 0 : N_{\text{frames}} - 1$ **do**
- 3: $E^{(k)} \leftarrow \emptyset$
- 4: **for** each path $p \in P$ **do**
- 5: Predict $\hat{\mathbf{t}}_p^{(k+1)}$ from p using (8)
- 6: Find $S \subseteq T^{(k+1)}$ within ϵ_{track} of $\hat{\mathbf{t}}_p^{(k+1)}$
- 7: $E^{(k)} \leftarrow E^{(k)} \cup \{(p, \mathbf{t}^{(k+1)}) \mid \mathbf{t}^{(k+1)} \in S\}$
- 8: $M^{(k)} = \text{SolveAP}(P^{(k)}, T^{(k+1)}, \widehat{\text{dist}}, \widehat{\mathcal{M}})$ with \mathcal{M} as in (7) and $\widehat{\text{dist}}$ as in (9)
- 9: **for** each edge $(p, \mathbf{t}^{(k+1)}) \in M^{(k)}$ **do**
- 10: Replace $p \in P$ by p with $\mathbf{t}^{(k+1)}$ appended
- 11: Remove $\mathbf{t}^{(k+1)}$ from $T^{(k+1)}$
- 12: $P \leftarrow P \cup \{[\mathbf{t}^{(k)}] \mid \mathbf{t}^{(k)} \in T^{(k)}\}$

at line 12, the set of paths P is extended with new paths containing singleton paths $[\mathbf{t}^{(k+1)}]$ of targets in $T^{(k+1)}$ not covered by $M^{(k)}$.

4 RECONSTRUCTION OF 3D TRAJECTORIES

Each camera in our studies accumulates a collection of paths in image coordinates as outlined in Section 3. The problem, then, is to match image paths captured by each camera to produce three-dimensional trajectories. For convenience, we refer to the two cameras as Camera I and Camera II and we refer to the associated sets of image paths produced by Algorithm 1 as P_I and P_{II} respectively. The cameras are calibrated so that their intrinsic and extrinsic parameters, including the location and orientation of Camera II relative to Camera I, are known. The calibration process is discussed in section 5.1. We sketch the essential procedure in Algorithm 2 and fill in the details in Sections 4.1 and 4.2.

The result of Algorithm 2 is a set C of curved trajectories consisting of three-dimensional world coordinates of points. Actually, since each point on the trajectory is matched to a particular video frame k , we store the image frame k and a measure of error $d^{(k)}$ with the world coordinates $\mathbf{r}^{(k)}$ of each point in the computed trajectory.

4.1 Reconstructing World Coordinates

Given a pixel (u_I, v_I) in image coordinates captured by Camera I, it is straightforward to determine a line

Algorithm 2: Reconstructing trajectories in 3D.

Input: Collections of image paths P_I and P_{II} captured by Camera I and Camera II respectively
Output: Set C of trajectories in three dimensions

- 1: $C \leftarrow \emptyset$
- 2: **for** $p_I \in P_I$ **do**
- 3: **for** $p_{II} \in P_{II}$ **do**
- 4: $K \leftarrow$ set of common frames of p_I and p_{II}
- 5: **if** $|K| > K_{\text{min}}$ **then**
- 6: $c \leftarrow \emptyset$
- 7: **for** $k \in K$ **do**
- 8: Select $\mathbf{t}_I^{(k)}$ from p_I , $\mathbf{t}_{II}^{(k)}$ from p_{II}
- 9: Back-project $\mathbf{t}_I^{(k)}$ onto line $\ell_I^{(k)}$
- 10: Back-project $\mathbf{t}_{II}^{(k)}$ onto line $\ell_{II}^{(k)}$
- 11: Find distance $d^{(k)}$ between $\ell_I^{(k)}$ & $\ell_{II}^{(k)}$
- 12: Find midpoint $\mathbf{r}^{(k)} \in \mathbb{R}^3$
- 13: Append tuple $(k, \mathbf{r}^{(k)}, d^{(k)})$ onto c
- 14: $C \leftarrow C \cup \{c\}$
- 15: Define $\widehat{\text{dist}}(p_I, p_{II}) =$ average of $d^{(k)}$
- 16: $M = \text{SolveAP}(P_I, P_{II}, \widehat{\text{dist}}, \mathcal{M})$ with \mathcal{M} as in (7) and $\widehat{\text{dist}}$ as above

$\ell_I \subseteq \mathbb{R}^3$ for which every point in the line is projected onto the pixel (u_I, v_I) by Camera I. The details required to compute a representation of ℓ_I involve homogeneous coordinates and Camera I's intrinsic and extrinsic parameters; see, e.g., (Hartley and Zisserman, 2004) for more details. The computation is identical for Camera II, so, lines 9 and 10 of Algorithm 2 simply refer to this procedure as “back-projecting” the pixels $\mathbf{t}_I^{(k)}$ and $\mathbf{t}_{II}^{(k)}$ onto the spatial lines $\ell_I^{(k)}$ and $\ell_{II}^{(k)}$ respectively.

Given representations of the lines $\ell_I^{(k)}$ and $\ell_{II}^{(k)}$, it is elementary to find the shortest distance $d^{(k)}$ between the two lines. We refer to the world coordinates of the midpoint of the corresponding line segment between the two closest points on either line as $\mathbf{r}^{(k)}$. Presumably, if two back-projected lines actually intersect, the computed error $d^{(k)}$ would be zero; as such, the distance $d^{(k)}$ is a reasonable proxy for the error in using $\mathbf{r}^{(k)}$ as the supposed spatial point that corresponds to image points $\mathbf{t}_I^{(k)}$ and $\mathbf{t}_{II}^{(k)}$ simultaneously.

The tentative curves in world coordinates are accumulated in line 13 of Algorithm 2. These curves consist of the midpoints $\mathbf{r}^{(k)}$ as described above. The frame coordinate k and the length $d^{(k)}$ are stored also (the latter providing a measure of pointwise error).

4.2 Matching Image Paths to Space Curves

After the space curves are built up in Algorithm 2, it

remains to figure out which paths in P_I and P_{II} actually do correspond to a physically reasonable curve c in 3D. The construction of a distance function dist at line 15 can be used to set up another assignment problem. The function $\overline{\text{dist}}(p_I, p_{II})$ computes the average value $d^{(k)}$, i.e.,

$$\bar{d} = \frac{1}{|K|} \sum_{k \in K} d^{(k)}, \quad (10)$$

where K is the set of common frames of p_I and p_{II} . For paths p_I and p_{II} deemed obviously incompatible, $\overline{\text{dist}}(p_I, p_{II}) = \infty$.

The metric defined in (10) allows us to solve another final assignment problem to figure find a matching of paths from either camera (and hence the desired three-dimensional trajectories). Again, rather than assume that one of the sets P_I or P_{II} must be covered, the set $\mathcal{M} \subset \mathcal{P}(P_I \times P_{II})$ has a more subtle definition. Any matching $M \in \mathcal{M}$ has the property that, for any edges (p_I, p_{II}) such that $\overline{\text{dist}}(p_I, p_{II}) < \infty$, one of p_I or p_{II} is covered by M (as in (7)).

5 EXPERIMENTS AND ANALYSIS

Our experimental apparatus consists of two video cameras because real-world coordinates of the flight paths cannot be obtained by a single camera. However, the two-dimensional images provided by a single camera still provide useful qualitative information. For instance, it is plainly visible that gravity plays an important role in blood droplets' curved trajectories even at small distances. This observation brings into question the validity of the stringing method for inferring the location of the blood-letting event. Furthermore, we can later combine the two-dimensional information from both cameras to build accurate three-dimensional trajectories with real-world measurements.

5.1 Experimental Setup

Figure 3 shows our experimental setup. The experiments are set up on a steel table with dimensions roughly 0.9×3.0 m. Plywood boards with a white vinyl finish are placed along the two edges opposite to the stereo camera pair. These boards act as walls to contain the splatter and to provide a uniform background for the experiments¹. The target is a thin latex packet containing 20 ml of transfer blood encased in

¹Different surfaces can be clamped onto the walls to study blood-surface interaction responsible for bloodstain pattern formation. We plan to study this issue in the future.



Figure 3: Experimental setup showing ballistic gel containing transfer blood. Experiments are captured using a stereo camera pair capable of recording high-speed video.

gelatin designed to approximate human flesh. The target is raised off the table with a lab jack. The paintball gun sits directly behind the target.

Two high-speed cameras, protected by sheets of Plexiglas, record the experimental setup from two viewpoints, capturing videos necessary to reconstruct the blood droplets' trajectories in 3D. In the following discussion, we will refer to them as the *frontal* and *lateral* cameras, in reference to their position around the experiment table. Fourteen 500 W work lights illuminate the scene, allowing cameras to capture videos at 1300 frames per second. A triggering mechanism controls the two cameras to capture synchronized videos. Each experiment begins by recording the calibration rig—a flat checkerboard pattern—moving through the cameras' fields of view. These calibration videos are used to compute each individual camera's intrinsic and extrinsic parameters (Hartley and Zisserman, 2004). Once calibrated, the cameras are configured to record the experimental area at high speed and the gun is fired. Upon impact with the target, the latex container breaks, causing the gel and the liquid to escape and leaving "bloodstains" on the wall. The process typically takes anywhere from 0.6 to 1.3 seconds, producing up to 1690 grey-scale frames from each camera. Video resolution is 1280×800 pixels.

Our system has a very low threshold for errors, so we devised the following calibration scheme. We point a laser at the scene and record a pair of videos showing the laser dot moving through the scene. The position of the laser dot in each video frame can then be used to verify the camera pair calibration (see Figure 4). A modified version of the segmentation procedure from Section 2.2 is used to detect the laser dot; only the brightest region is kept if the segmentation finds more than one connected component. We assume that the location and direction of the cameras do not change during the course of the experiment, i.e., that the extrinsic parameters computed during the calibration process do not change. The laser verifica-

tion procedure described above is repeated after each experiment to validate the preceding assumption.

A failure in the second laser verification signals that at least one of the cameras moved during the experiment. This could happen due to kinetic energy being transferred to the walls or the camera base by recoil from the gun or the bullet bouncing off the walls. In either case, the experiment is discarded as we cannot use visual cues from the experiment table to compensate for this movement.

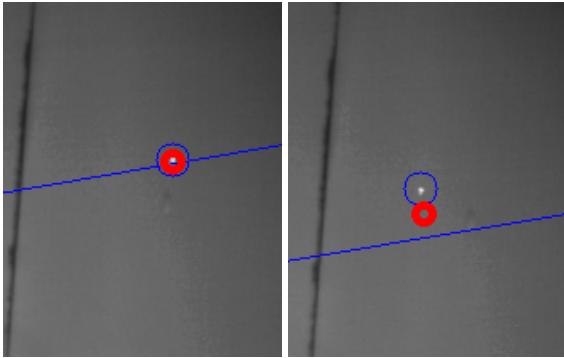


Figure 4: Calibration verification by shining a laser at the observed region. In these figures, thin blue circles depict the laser dot, blue lines represent the epipolar line corresponding to the laser dot in the other camera, and the thick red circles show the re-projection of the 3D reconstruction of the laser dot. The left image shows a successful calibration. Here, the epipolar line crosses the laser dot and the re-projection coincides with the original location. The right image shows an inaccurate calibration. One of the cameras has moved, perhaps due to the vibrations generated by the recoil of the gun.

A few pictures of the bloodstains are captured before cleaning up the lab and preparing for the next experiment. These pictures are taken using similar equipment and techniques available to a forensic investigator capturing photographic evidence of bloodstains at a crime scene. 48 successful experiments were conducted.

5.2 Validation by Visual Inspection

A single video from an experiment yields hundreds of image paths from each camera. It is infeasible to track more than a few trajectories manually, far fewer than would be required to obtain a statistically representative sample of the entire set of trajectories. Furthermore, correlating trajectories tracked by hand to ones tracked automatically by our system would require a scheme to account for quantitative differences between clusters of pixels identified subjectively by a human operator versus those segmented automatically by the scheme outlined in Section 2.2. Thus, we

need a way to allow the operator to quickly track and compare hundreds of tracks simultaneously, sacrificing the quantitative measure of how many paths and how many false paths were found.

We have developed a tool that allows a user to explore tracking performance visually. The video is played back at a lower frame-rate, overlaid with partial trajectories (see the middle image of Figure 1). Only the currently active trajectories—those that have started but have not yet ended in the current frame—are shown, and only the path segments up to the current frame. The overall effect is that the trajectories appear to be following the droplets, allowing the operator to focus the attention on a group of moving droplets and evaluate the correctness of the paths. This tool was improved to show the predicted position and search window in subsequent frames as an aid to evaluate the accuracy of the predictions.

5.3 Validation by Counting Matches

Ideally, the process described in sections 2.1 to 3.3 should return the paths of all droplets and no spurious or erroneous paths. In this event, every image path detected by the frontal camera corresponds to an image path detected by the lateral camera. In actual experiments, some droplets are not detected by one or both cameras, one or both cameras may register image targets that are false positives, and some droplets may be visible by only one of the cameras in some frames. In all of these cases, the matching algorithm should not match image paths between the cameras' respective videos.

Table 1: Number of matching paths for three of the experiments and cumulative result for the 48 experiments conducted.

N.	Frontal	Lateral	Matches	Accuracy
1	368	281	233	82.9 %
2	416	327	235	71.9 %
3	598	270	203	75.2 %
T	25542	9769	8534	87.4 %

The first three rows of Table 1 show the matching results for three experiments. The first column simply labels the experiments; the last row being a summary over all 48 experiments conducted. The *Accuracy* column is computed as the ratio between the number of paths detected by the camera that found the least amount of tracks (in these cases, the lateral camera) and the number of matches.

Figure 5 images with paths overlaid from the least accurate experiment from Table 1. As the front-facing camera detected more paths than the lateral camera (which suggests that it has a better view of the exper-

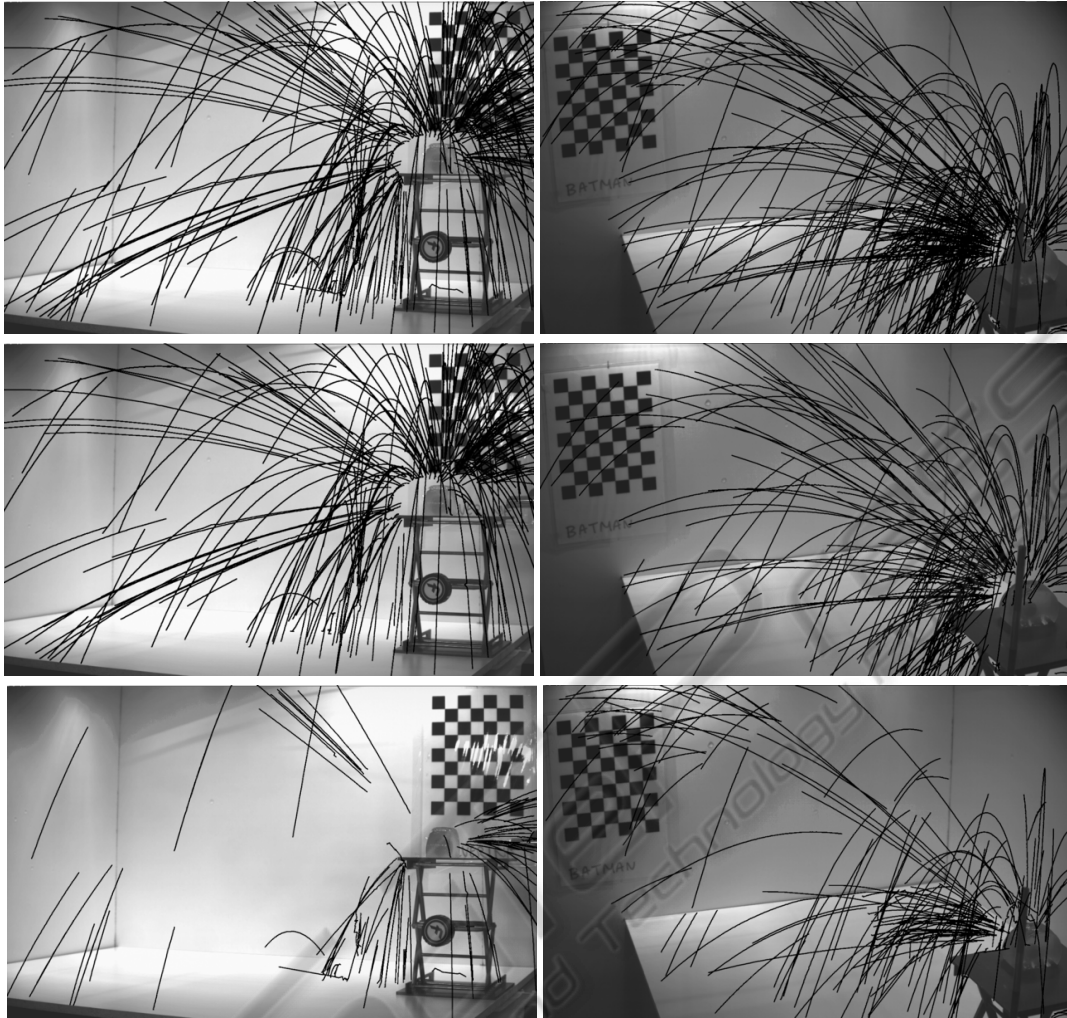


Figure 5: 3D matching. Left column: lateral camera. Right column: front-facing camera. Top row: all paths. Middle row: matched paths. Bottom row: discarded paths. The paths were drawn on top of the first video frame to give an idea of the relative location and orientation of the cameras.

iment), we necessarily discarded more paths from the front view than from the lateral view. Of the paths discarded from the lateral view (bottom row of Figure 5), most were travelling backwards or downwards from the initial position of the target, i.e., toward regions outside the view of the frontal camera. Therefore, the apparent poor matching in this particular experiment from Table 1 can be accounted for by paths partially hidden from one of the cameras. It is also worth noting that some of the discarded paths match very closely to their own shadows (this can be seen in the short path near the centre of the lower left image).

Figure 6 shows the reconstruction errors for all points and paths obtained in the 48 experiments. The left histogram plots the error (in cm) on the horizontal axis against the number of points on the vertical axis. The right-hand histogram shows the same pa-

rameters again, but with maximum errors for each path versus the number of paths. For most of the reconstructed points, the reconstruction error is lower than 5 mm. Figure 7 shows the 3D reconstructions for Experiments 1 and 2.

5.4 Validation by Inferring Parameters

If we assume constant acceleration, the position of a droplet at time τ is given by

$$\mathbf{p}(\tau) = \begin{pmatrix} p_x(\tau) \\ p_y(\tau) \\ p_z(\tau) \end{pmatrix} = \mathbf{p}(0) + \mathbf{v}(0)\tau + \frac{\mathbf{a}}{2}\tau^2. \quad (11)$$

This model is not completely accurate as it ignores viscous effects. However, (11) can still be used to compute a rough estimate of the gravitational constant

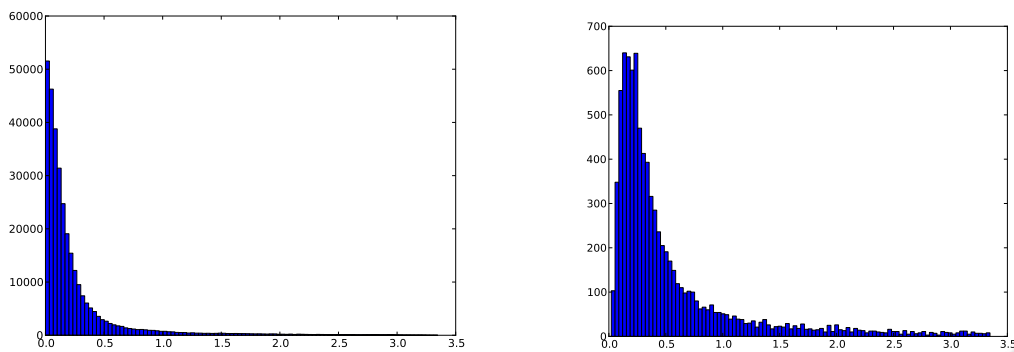


Figure 6: Error histograms. Left: Error in cm (horizontal axis) vs. the number of points (vertical axis). Right: Number of paths (vertical axis) vs. maximum error in these paths.

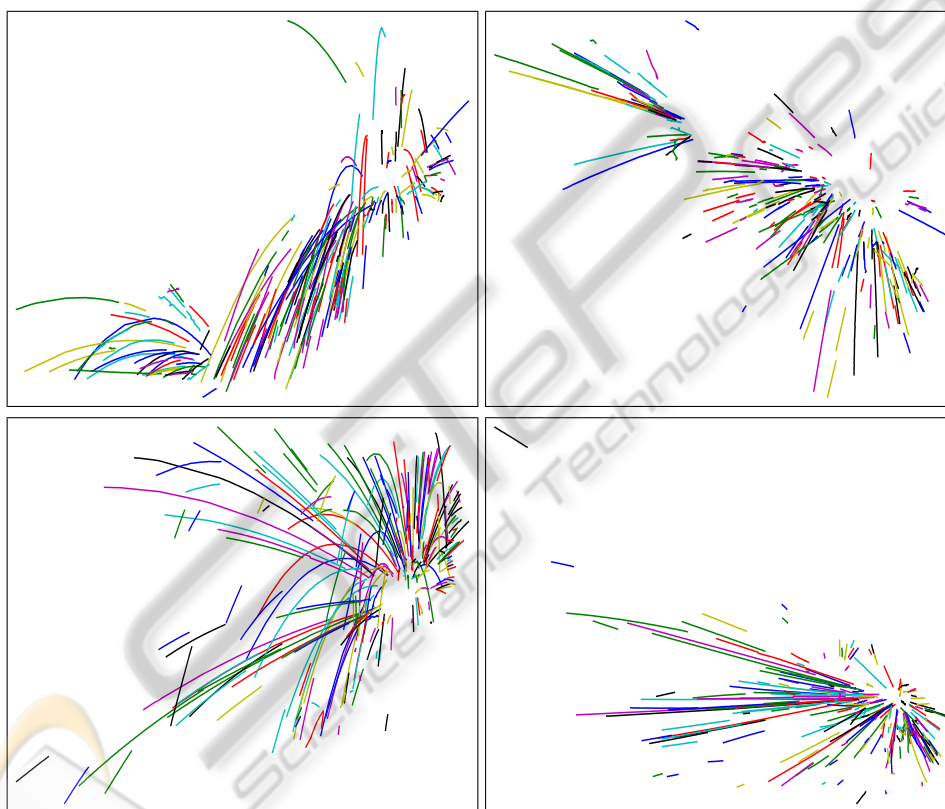


Figure 7: 3D reconstruction of experiments 1 (top) and 2 (bottom). Left: lateral view. Right: top view.

$g \approx 9.8 \text{ m/s}^2$. Notice we that we cannot use g directly in our model-based prediction of image paths because the parabolic paths constructed using Algorithm 1 because the paths constructed there are in image coordinates.

From the frame-rate and our tracking data, we know the locations $\mathbf{p}(\tau)$ and times τ . Similarly as in Section 3.3, we can fit each component of the data points $\mathbf{p}(\tau)$ with a parabola:

$$\mathbf{p}(\tau) \approx \mathbf{d} + \mathbf{e}\tau + \mathbf{f}\tau^2. \quad (12)$$

From (11) and (12), we can estimate the accelerations as $\mathbf{a} \approx 2\mathbf{f}$. When a droplet is ascending, both the force of gravity and the drag force point downward. Conversely, when a droplet is descending, the force of gravity opposes the drag force. Thus, if we compute the accelerations independently for upward and downward portions of the trajectories, we should obtain a greater magnitude for the vertical components of acceleration in the first case than in the second.

Table 2 summarizes the mean vertical accelera-

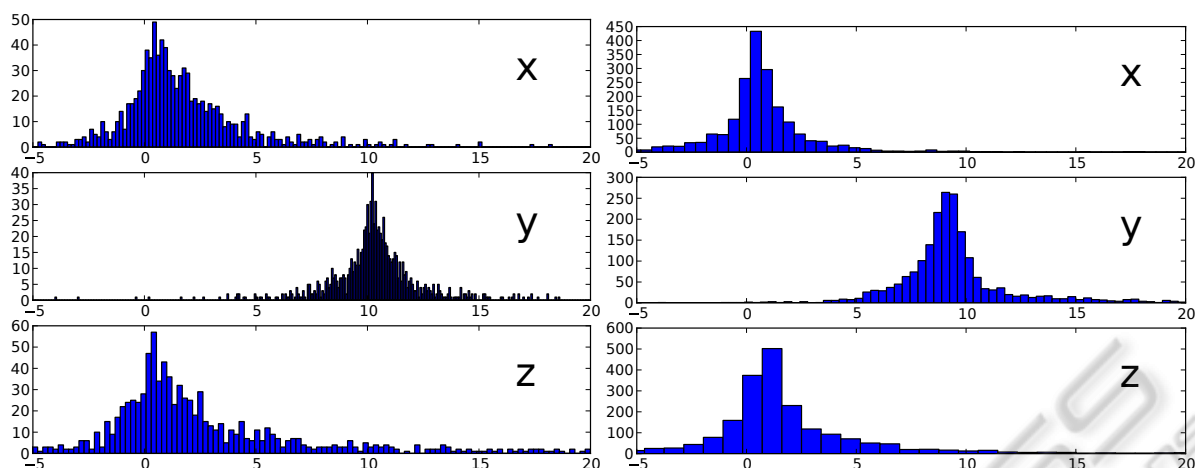


Figure 8: Accelerations (in m/s^2) computed from the 3D reconstruction. Left: using only the upwards portions of the paths. Right: using only the downwards portions of the paths.

Table 2: Estimated value of g inferred from the paths, using only the upwards portions, the downwards portions, and all the points in the path, respectively. A constant acceleration was assumed. Only sections of paths with at least 30 measurements are used to compute these values. The number of paths that had more than 30 measurements in each direction are indicated in parentheses.

N. (up / down / all)	Up	Down	Total
1 (19 / 111 / 120)	9.09	9.03	9.08
2 (69 / 62 / 124)	10.41	9.13	9.85
3 (37 / 31 / 69)	9.93	7.84	9.04
T (1214 / 2486 / 3545)	10.36	10.24	10.36

tions obtained from the three experiments. Note that the value is consistently greater in the upwards portions than in the downwards portions, as expected.

Figure 8 is a histogram of the acceleration components associated with each path extracted by the experiments. Despite having obtained a good approximation of g in the second row, the variance of the computed values for the three axis shows that the effect of drag forces is not negligible and should be taken into account when analyzing bloodstain patterns in crime scenes.

6 CONCLUSIONS

We apply computer vision techniques to estimate parameters needed to describe blood droplet flight paths caused by a violent event accurately. This paper represents the first step toward that goal: estimating 3D trajectories of blood droplets using a stereo camera setup. The system described here uses model-based tracking to estimate trajectories of image features captured by individual cameras. The 2D image trajec-

tries are then matched across the two cameras to reconstruct 3D trajectories in world coordinates. In a given experiment, any proposed system needs to track hundreds of droplets simultaneously; therefore, manual annotation of ground truth to determine the performance of the proposed algorithm is infeasible. Instead, we have developed three novel strategies for indirectly measuring the performance of our system. The initial results appear promising.

Several extensions of this work are currently in progress. From our results, it is obvious that air resistance and gravity play a significant role in how blood droplets move through the air even at short distances. We are currently developing physics-based models incorporating the influence of gravity and aerodynamic drag to describe blood droplet trajectories. The data acquired by the system described here can validate putative physics-based motion models under development and determine the relative magnitude of the forces ignored in stringing-based methods. Beyond modelling droplet flight, it is necessary to investigate robust methods based on a validated model for backtracking from a bloodstain to the original source.

REFERENCES

- Balch, T., Khan, Z., and Veloso, M. (2001). Automatically tracking and analyzing the behavior of live insect colonies. In *AGENTS '01*, pages 521–528. ACM.
- Betke, M., Hirsh, D. E., Bagchi, A., Hristov, N. I., Makris, N. C., and Kunz, T. H. (2007). Tracking large variable numbers of objects in clutter. In *CVPR '07*, pages 1–8. IEEE.
- Bevel, T. and Gardner, R. M. (2008). *Bloodstain Pattern Analysis With an Introduction to Crimescene Reconstruction*. CRC Press, 3rd edition.

- Bijsterbosch, J. and Volgenant, A. (2010). Solving the rectangular assignment problem and applications. *Ann. Oper. Res.*, 181:443–462.
- Bourgeois, F. and Lassalle, J.-C. (1971). An extension of the Munkres algorithm for the assignment problem to rectangular matrices. *Commun. ACM*, 14:802–804.
- Bradski, G. (2000). The OpenCV Library. *Dr. Dobbs J.*
- Buck, U., Kneubuehl, B., Näther, S., Albertini, N., Schmidt, L., and Thali, M. (2011). 3D bloodstain pattern analysis: Ballistic reconstruction of the trajectories of blood drops and determination of the centres of origin of the bloodstains. *Forensic Sci. Int.*, 206(1-3):22–28.
- Dasgupta, D., Hernandez, G., Garrett, D., Vejandla, P. K., Kaushal, A., Yerneni, R., and Simien, J. (2008). A comparison of multiobjective evolutionary algorithms with informed initialization and Kuhn-Munkres algorithm for the sailor assignment problem. In *GECCO '08*, pages 2129–2134. ACM.
- Grover, D., Tower, J., and Tavaré, S. (2008). O fly, where art thou? *J. Roy. Soc. Interface*, 5(27):1181–1191.
- Hartley, R. and Zisserman, A. (2004). *Multiple view geometry in computer vision*. Cambridge University Press, 2nd edition.
- Iwase, S. and Saito, H. (2004). Parallel tracking of all soccer players by integrating detected positions in multiple view images. In *ICPR 2004*, volume 4, pages 751–754. IEEE.
- Khan, Z., Balch, T., and Dellaert, F. (2003). Efficient particle filter-based tracking of multiple interacting targets using an MRF-based motion model. In *IROS 2003*, volume 1, pages 254–259. IEEE.
- Khan, Z., Balch, T., and Dellaert, F. (2005a). MCMC-Based Particle Filtering for Tracking a Variable Number of Interacting Targets. *IEEE Trans. Pattern Anal. Mach. Intell.*, 27(11):1805–1918.
- Khan, Z., Balch, T., and Dellaert, F. (2005b). Multitarget tracking with split and merged measurements. In *CVPR '05*, volume 1, pages 605–610. IEEE.
- Kuhn, H. (1955). The Hungarian Method for the assignment problem. *Nav. Res. Logist.*, 2(1-2):83–97.
- Munkres, J. (1957). Algorithms for the Assignment and Transportation Problems. *SIAM J. Appl. Math.*, 5(1):32–38.
- Nillius, P., Sullivan, J., and Carlsson, S. (2006). Multi-Target Tracking—Linking Identities using Bayesian Network Inference. In *CVPR '06*, volume 2, pages 2187–2194.
- Poore, A. B. and Gadaleta, S. (2006). Some assignment problems arising from multiple target tracking. *Math. Comput. Model.*, 43(9-10):1074–1091.
- Reid, D. (1979). An algorithm for tracking multiple targets. *IEEE Trans. Autom. Control*, 24(6):843–854.
- Straw, A. D., Branson, K., Neumann, T. R., and Dickinson, M. H. (2011). Multi-camera real-time three-dimensional tracking of multiple flying animals. *J. Roy. Soc. Interface*, 8(56):395–409.
- Veenman, C., Reinders, M., and Backer, E. (2001). Resolving motion correspondence for densely moving points. *IEEE Trans. Pattern Anal. Mach. Intell.*, 23(1):54–72.
- Yilmaz, A., Javed, O., and Shah, M. (2006). Object tracking: A survey. *ACM Comput. Surv.*, 38(4).